

A synergistic approach to optical modeling of PCSELs through rigorous methods and the coupled-wave theory

A. Bisianov^{1,2} and A. Waag^{1,2}

¹*Institute of Semiconductor Technology, Technische Universität Braunschweig, Braunschweig 38106, Germany*

²*Nitride Technology Center (NTC), Technische Universität Braunschweig, Braunschweig 38106, Germany*

(*Electronic mail: a.bisianov@tu-braunschweig.de)

(Dated: 2 March 2026)

A wide range of numerical and semi-analytical approaches has been developed for optical modeling of photonic-crystal surface-emitting lasers (PCSELs). However, a systematic framework for comparing their predictive capabilities and identifying their respective validity limits remains largely unexplored. In this work, we introduce a comparative methodology in which four representative methods—including rigorous numerical and effective-index-based approaches—are analyzed and partially hybridized within a coupled-wave-theory framework. Using single-lattice and double-lattice PCSELs as representative models, we demonstrate that this approach not only reveals fundamental differences between predictions of rigorous numerical methods and the coupled-wave-theory framework, but also captures a qualitative phase transition and a symmetry-broken phase of quasi-bound states in the continuum (quasi-BICs) relevant for laser operation.

INTRODUCTION

First proposed in 1999^{1,2}, photonic-crystal surface-emitting lasers (PCSELs) have evolved into a rapidly advancing chip-scale technology^{3–10}. They continue to push the performance limits of conventional semiconductor lasers, particularly in terms of brightness, beam quality, and emission directionality.

Alongside these technological advances and the growing diversity of PCSEL platforms, a wide range of electro-optical design approaches and numerical tools has been developed. Among the most established semi-analytical methods is the three-dimensional coupled-wave theory (3D-CWT), which enables the analysis of both infinitely periodic and finite PCSEL structures and was originally formulated in Refs.^{11–14}. Subsequently, this framework was extended to more complex and optically powerful photonic-crystal geometries, most notably the double-lattice photonic crystal (PhC)^{15–19}. Time-dependent version of 3D-CWT, incorporating carrier-photon interactions and nonuniform temperature profiles, has also been developed and applied^{20–23}. Beyond PCSEL designs based on highly symmetric nanostructures, such as cylindrical air holes, 3D-CWT has also been employed to investigate PCSELs with more asymmetric geometries, including triangular holes^{24–26}, rotatable double-ellipse patterns²⁷, and structures with tilted sidewalls²⁸ or spatially varying hole depths^{15,29,30}.

Despite its widespread adoption and versatility, the semi-analytical 3D-CWT is not the only numerical approach developed in recent years for PCSEL design. For instance, several studies have employed rigorous coupled-wave analysis (RCWA)^{31–33}, which enables accurate calculations of resonant frequencies, quality factors, and optical field distributions, as well as related laser performance metrics. More recently, Persson et al. introduced the k-space weighted loss estimation (kSWLE) approach³⁴, which allows for accurate evaluation of both vertical and lateral optical losses of lasing modes and thus provides an alternative to finite-size

implementations of 3D-CWT. Loss estimation in finite PCSELs has also been addressed using a probabilistic Markov chain model, as proposed in Ref.^{35,36}. Another study particularly relevant to the present work compares several effective-index-based approaches³⁷, including the so-called iterated effective-index method (I-EIM), with fully three-dimensional numerical methods, namely RCWA and the transmission-line method (TLM). In addition, fully three-dimensional simulations based on the finite-element method (FEM)—as implemented in COMSOL Multiphysics—have also been applied to PCSELs, for example, in Ref.³⁸.

Although both effective-index-based and fully three-dimensional methods have been extensively developed and applied to PCSELs, a systematic comparative analysis that identifies qualitative differences in their predictions and explores their potential for predictive synergy remains lacking. In this article, we introduce such a comparative scheme, wherein rigorous numerical methods are employed as "phenomenological" inputs within a generalized coupled-wave theory framework. Since this framework incorporates explicit input from a chosen rigorous method, it can also be regarded as a hybridized CWT framework. While the proposed technique is, in principle, applicable to a wide variety of PCSEL types, it is demonstrated here using two otherwise well-studied configurations.

Specifically, this article compares two rigorous three-dimensional methods—namely the finite-element method (FEM) and rigorous coupled-wave analysis (RCWA), also known as the Fourier modal method (FMM)—with two effective-index-based approaches, including the widely used 3D-CWT and the recently proposed iterated effective-index method (I-EIM). These methods are applied to blue gallium nitride (GaN)-based PCSELs, closely resembling watt-class devices reported in Ref.¹⁷. Two PCSEL variants operating at $\lambda \approx 430$ nm are considered: structures incorporating subwavelength-thin photonic-crystal (PhC) layers with either single-lattice or double-lattice patterns of circular air holes,

embedded in bulk GaN. In both cases, the PhC patterns are arranged on a periodic square lattice with a period of $a = 174$ nm, as illustrated in Figs. 1(a,b). Despite our focus on these specific square-lattice types, the comparative framework introduced here can be readily extended to a broader class of lattice types and PhC patterns.

The remainder of this article is organized as follows. In the first section, we introduce the two PCSEL configurations in detail. The subsequent section is devoted to the methodological aspects of the numerical approaches considered. As will become evident, all four methods provide full or partial access to key optical characteristics, including resonant frequencies and quality factors of transverse-electric (TE) modes relevant for lasing operation, as well as the associated photonic-crystal (PhC) confinement factors. In addition, microscopic parameters governing in-plane and out-of-plane optical feedback are extracted from FEM, FMM, and, to a limited extent, I-EIM by invoking a generalized coupled-wave theory (CWT)^{11,12,18}. In contrast, within 3D-CWT, these quantities are derived directly from first principles. In this way, we enable a comparison of rigorous and effective-index-based methods on a common basis within the generalized CWT framework. In the following section, we present numerical results for PCSEL platforms featuring two PhC pattern variations and discuss the relative accuracy of each method, along with the validity limits of the generalized CWT framework. The final section summarizes the main findings.

I. TWO PCSEL MODELS AND QUASI-BIC STATES

In this section, we introduce the two aforementioned types of square lattice as illustrated in Fig. 1(a,b). The simplest single-lattice, which features one cylindrical air hole of diameter d per lattice unit cell, will be further referred to as Type I. The PCSEL as a whole and the PhC layer, incorporating such a pattern, will be equally called Type I later on. By definition, air hole filling factor ff is defined via the hole diameter as $\pi d^2/(4a^2)$, where a is the lattice period of the square unit-cell $a \times a$. We fix a to 174 nm throughout this study, thus tuning the Bragg resonance wavelength $\lambda_{\text{Bragg}} \approx a * n_{\text{eff}}$ to around 430 nm. An optimal PhC thickness t_{PhC} lies in the order of half-wavelength in the material, which is $\lambda_{\text{Bragg}}/(2n_{\text{eff}}) \sim 100$ nm. Therefore, the thickness is fixed to 100 nm in both PCSEL types. Additionally, we probe a variety of PhC thicknesses in the Type I case.

Next, a basic double-lattice PhC features two cylindrical holes of diameters d_1 and d_2 , respectively. For convenience, we refer to this pattern as Type II. The corresponding hole filling factors are ff_1 and ff_2 . The lateral distance between the holes along the x and y axes is defined as $\Delta = \Delta_x = \Delta_y$ as shown in Fig. 1(b). In our parametric study, we ensure that $\Delta < (d_1 + d_2)/(2\sqrt{2})$, thus preventing the holes from merging.

To make the two PCSEL types comparable, both Type I and Type II PhC layers are embedded in the same GaN-based epitaxial multilayer stack, which is introduced in Table I. As already mentioned, the multilayer stack under study closely

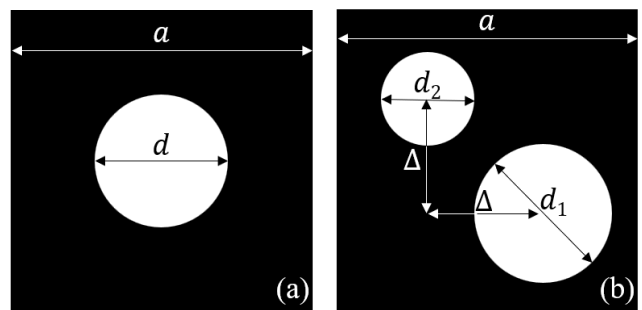


FIG. 1. Refractive-index profile of a unit cell of the single-lattice (left) and double-lattice (right) photonic crystals. White regions correspond to air holes, while black regions denote bulk GaN.

resembles blue PCSELS realized in¹⁷. The presented PCSEL platform has not been intentionally optimized as an ultimate design proposal and serves here as merely a realistic study model. Neither the optical losses associated with material absorption nor the optical gain of the active region are included in our model. Additionally, the top p-type electrode pad has been omitted since the ITO layer of 200 nm proved to be sufficiently thick to optically isolate fundamental guided modes of interest. Having said that, it is important to keep in mind that a p-type electrode can act as an optical reflector, which redirects and redistributes the optical field, thus leading to a significant modification of upward and downward radiation rates $\alpha_{\text{up,down}}$ of a lasing device (on that matter see e.g.^{17,30,39}). Here, we do not take into account or make an accent on such effects, since power maximization and laser performance optimization are beyond the scope of this study. Moreover, we do not take into account any finite-size effects, such as, e.g., in-plane optical losses, assuming a periodically infinite PCSEL in the lateral xy -plane.

Throughout this study, we concentrate on four fundamental quasi-TE modes that are common to both Types I and II PhC patterns and are well established in the literature^{3,11,18}, as the most relevant modes in standard PCSELS with TE-polarized optical gain. These eigenmodes and their associated photonic bands are conventionally denoted as A, B, C, and D, with their fourfold multiplicity originating from the rotational C_4 symmetry of the underlying square lattice. In a broader context of photonic-crystal theory, band-edge modes A and B with zero in-plane quasimomentum (i.e., at the central Γ point of the reciprocal space) are classified as symmetry-protected bound states in the continuum (BIC)⁴⁰⁻⁴³. These states exhibit infinite quality factors, as they do not couple to free-space radiation owing to their symmetry mismatch with existing radiative channels. In theory, the symmetry-protected BICs are immune to perturbations preserving the underlying symmetry of the lattice, which is the case for the Type I lattice with one circularly symmetric hole. In contrast, the two holes of the Type II lattice break the rotational C_4 symmetry of the square lattice, thus lifting the symmetry protection and forcing the band-edge BIC states A and B to radiate at the Γ point. In real devices, fabrication-induced distortions of the PhC pattern render the Q factors of modes A and B finite, even for the

TABLE I. Layer properties of the modeled PCSEL stack, featuring either single-lattice (Type I) or double-lattice (Type II) PhC.

Layer material	Thickness [nm]	Refractive index
ITO	200	2.02
p-GaN	25	2.5
p-AlGaIn	400	2.47
p-AlGaIn	15	2.42
ud-GaN	130	2.5
ud-InGaIn	3	2.73
ud-GaN	6	2.5
ud-InGaIn	3	2.73
ud-GaN	6	2.5
ud-InGaIn	135	2.51
PhC	100	2.5 (bulk), 1 (hole)
n-GaN	80	2.5
n-AlGaIn	2000	2.47
n-GaN substrate	—	2.5

Type I lattice. In that case, the more precise term "quasi-BIC state" is used, accounting for a weak power leakage into free space. As will be evident from the numerical results presented below, rigorous simulations likewise yield finite Q factors. Moreover, the numerical data show for the Type I PCSEL that the radiation constants $\alpha_{A,B}$, which are inversely proportional to the respective Q-factors, are exponentially growing with the hole filling factor ff . This suggests that a certain symmetry-protection effect takes place only at sufficiently small hole diameters.

II. METHODOLOGY

In this section, we describe four methods applied to the earlier introduced PCSEL configurations. The first pair of methods is the aforementioned finite element method (FEM) and the rigorous coupled-wave analysis (RCWA), which is also called the Fourier modal method (FMM). They are implemented via commercially-available COMSOL Multiphysics and Ansys Lumerical software, respectively. The second pair of methods is the semi-analytical effective-index-based 3D-CWT^{11,12,18}, and I-EIM³⁷ approaches, introduced earlier in the text. In contrast to rigorous methods, which evaluate electromagnetic fields as fully three-dimensional entities, the semi-analytical ones effectively homogenize the refractive index profile of the PhC layer, thereby enabling a separable representation of the electric field of the form $E_{1D}(z)E_{2D}(x,y)$. One of the main drawbacks of the 3D-CWT method is the assumption that the four fundamental quasi-TE modes share an identical vertical field profile $E_{1D}(z)$. As will be shown below, the I-EIM can, to some extent, mitigate this limitation. By contrast, FEM and FMM do not rely on this assumption and instead fully resolve the three-dimensional geometry of the PCSEL structure.

Despite these simplifying assumptions, 3D-CWT remains a valuable and instructive approach, as it enables an analytical derivation of so-called Hermitian $\hat{C}_{1D}, \hat{C}_{2D}$ and non-Hermitian \hat{C}_{rad} field coupling matrices, governed by the associated cou-

pling coefficients. In accordance with Ref.¹⁸, we utilize the following CWT-based system of nonlinear equations, which we hereafter refer to as the CWT framework:

$$\delta_{A,C} + i\alpha_{A,C}/2 = \kappa_{11} + \kappa_{2D+} + i\mu \quad (1)$$

$$\mp \sqrt{[(\kappa_{1D} + \kappa_{2D-}) + i\mu e^{i\theta_{pc}}] [(\kappa_{1D} + \kappa_{2D-})^* + i\mu e^{-i\theta_{pc}}]},$$

$$\delta_{B,D} + i\alpha_{B,D}/2 = \kappa_{11} - \kappa_{2D+} + i\mu \quad (2)$$

$$\mp \sqrt{[(\kappa_{1D} - \kappa_{2D-}) + i\mu e^{i\theta_{pc}}] [(\kappa_{1D} - \kappa_{2D-})^* + i\mu e^{-i\theta_{pc}}]}.$$

These equations explicitly relate the complex eigenvalues of the fundamental modes to the coupling coefficients that govern internal field dynamics and wave interactions. Here, δ_i denote deviations of the corresponding spatial eigenfrequencies from the Bragg wavenumber $\beta_0 = 2\pi/a$, which is conveniently expressed in cm^{-1} . The quantities $\alpha_i = \beta_0/Q_i$ represent the radiation constants associated with the respective modal quality factors. The in-plane distributed feedback of a PCSEL is governed by the coupling coefficients κ_{1D} and $\kappa_{2D\pm}$, which play a central role in determining lasing performance and optical losses. In the present study, we therefore focus primarily on these three key parameters.

Within the FEM and FMM methods, the spatial eigenfrequencies $\bar{\nu}_i = \beta_0 + \delta_i$ and the associated radiation constants α_i , are estimated as described in the corresponding subsections below. By contrast, our I-EIM formulation assumes a closed, lossless system and therefore does not provide access to radiation constants; consequently, only real-valued eigenfrequencies are obtained using this method.

For Type II PCSEL, only the real-valued coupling coefficient κ_{2D+} can be estimated based on I-EIM through:

$$\kappa_{2D+} = (\bar{\nu}_A - \bar{\nu}_B + \bar{\nu}_C - \bar{\nu}_D)/4 \quad (3)$$

In case of Type I PhC, 3D-CWT yields $\theta_{pc} = \pi$ and $\alpha_{A,B} = 0$, which reduces Eqs. (1,2) to

$$\delta_{A,B} = \kappa_{11} \pm 2\kappa_{2D} + \kappa_{1D}, \alpha_{A,B} = 0, \quad (4)$$

$$\delta_{C,D} = \kappa_{11} - \kappa_{1D}, \alpha_{C,D} = 4i\mu \quad (5)$$

and renders all coupling coefficients real-valued:

$$\kappa_{1D} = (\bar{\nu}_A + \bar{\nu}_B - \bar{\nu}_C - \bar{\nu}_D)/4, \quad (6)$$

$$\kappa_{2D+} = \kappa_{2D-} = (\bar{\nu}_A - \bar{\nu}_B)/4. \quad (7)$$

Therefore, besides 3D-CWT, I-EIM can also provide values for all these coefficients based on the associated real-valued eigenfrequencies. It should be emphasized that, according to the rigorous FEM and FMM, the condition $\alpha_{A,B} = 0$ must not be imposed a priori, as it generally breaks down at larger hole diameters, as will be demonstrated below. Accordingly, for

these methods, we employ the full form of the CWT framework given by Eqs. (1,2).

Next, within the CWT treatment¹⁸ of the Type II PhC, we define $\theta_{\text{pc}} = \pi + 2\arg(\xi_{1,0})$, where $\xi_{j,k}$ denote Fourier harmonics of the relative permittivity profile $\epsilon_{\text{PhC}}(x,y)$ of the PhC. As a consequence, the system of Eqs. (1,2) becomes overdetermined, comprising nine defined parameters but only seven unknowns. To resolve this issue, we fix the real-valued eigenfrequencies together with the radiation constants $\alpha_{\text{C,D}}$, while allowing the CWT framework to fit the remaining pair $\alpha_{\text{A,B}}$. This choice is not arbitrary, as the description of the quasi-BIC modes constitutes the key issue distinguishing predictions of rigorous methods from those of the CWT framework, as discussed in the following. At a heuristic level, this choice is further motivated by the observation that the 3D-CWT-based values of $\alpha_{\text{C,D}}$ generally exhibit better agreement with their counterparts based on FEM and FMM than the corresponding values of $\alpha_{\text{A,B}}$.

Finally, it is worth emphasizing that FEM- and FMM-based eigenfrequencies serve as a "phenomenological" input for the generalized CWT framework (Eqs. (1,2)), while 3D-CWT, being inherently constructed within the CWT framework, derives all coupling coefficients from first principles. The following subsections describe some specific aspects of each applied method.

A. Three-dimensional coupled-wave theory

The core algorithm of 3D-CWT is implemented as a code programmed in Wolfram Mathematica Software. The vertical electric field profile $E_{1\text{D}}(z)$ of the overall factorized electric field $E = E_{2\text{D}}(x,y)E_{1\text{D}}(z)$ is obtained via the Finite Difference Eigenmode (FDE) solver provided by Ansys Lumerical Software. The highest-order Fourier component of the PhC refractive-index profile is fixed to 11, so that the overall number of superimposed Bloch waves in the reciprocal space amounts to 22×22 . This number of harmonics ensures a decent numerical precision as well as an acceptable computational time, which typically does not exceed 30 min per run. Within the 3D-CWT method, radiative and high-order waves have been derived by applying the generalized or simplified Green functions described in^{11,12,28}. The use of simplified Green functions not only significantly reduces the computational cost but also avoids the emergence of nonphysical field divergences at relatively large PhC thicknesses, as will become evident for the Type I PCSEL. However, at least for a PhC thickness of 100 nm, the generalized Green functions do not exhibit a significant divergence; consequently, the generalized ansatz is employed within 3D-CWT for this thickness in both Type I and Type II PCSELS.

B. Iterated effective-index method

Next, the I-EIM method is implemented following Ref.³⁷. The effective two-dimensional field profile $E_{2\text{D}}(x,y)$ of a TE-polarized mode is obtained using the open-source software

package MPB⁴⁴, while its vertical field profile $E_{1\text{D}}(z)$ is calculated using the FDE solver provided by Ansys Lumerical Software. Within the I-EIM framework, these two field profiles are updated iteratively until convergence is achieved. As a convergence criterion, we require the relative change of the effective refractive index to satisfy $\Delta n_{\text{eff}}/n_{\text{eff}} < 10^{-5}$. In practice, three to five iteration steps are typically sufficient to meet this criterion.

In I-EIM, the electric field converges to only one of the four eigenmodes at a time ($i \in \{A,B,C,D\}$). Once the resonant wavelength λ_i of a selected mode is determined, the remaining three resonances follow directly from the two-dimensional eigenmode solver implemented in MPB. However, the resulting vertical field profile $E_{1\text{D}}(z)$ and consequently the photonic-crystal confinement factor Γ_{PhC} , can be uniquely associated only with the traced mode i . This constitutes a key difference from 3D-CWT, in which both the vertical electric-field profile $E_{1\text{D}}(z)$ and the PhC confinement factor defined as $\Gamma_{\text{PhC}} = \int_{\text{PhC}} \epsilon(z) |E_{1\text{D}}(z)|^2 dz$, are identical for all four modes. Note that Γ_{PhC} is defined as the fraction of the total field energy normalized to 100%. It is important to note that, unlike the FEM model of the PCSEL, the I-EIM model does not include absorber layers. Consequently, the resulting resonant eigenfrequencies are strictly real-valued, and the radiation constants cannot be estimated within this model.

In the present study, we trace only modes A and B, since these quasi-BIC states are most relevant for laser operation. After the traced wavelength λ_i and the three complementary resonances are obtained, the coupling coefficients $\kappa_{1\text{D}}, \kappa_{2\text{D}}$ are extracted from the generalized CWT framework. The two-dimensional coupling coefficients are subsequently normalized by the confinement factor Γ_{PhC} of the traced mode. The rationale for this renormalization is provided in the Appendix. All coupling-coefficient values reported in this study are based on tracing mode A. We have preliminarily verified that coupling coefficients obtained by tracing mode B differ only marginally from these values, with relative deviations not exceeding $\sim 2\%$ over the entire parameter range considered. This indicates a good self-consistency of the I-EIM method.

C. Finite element method

The first rigorous method employed in this study is the full three-dimensional FEM solver implemented in COMSOL Multiphysics. This approach computes stationary electromagnetic fields as intrinsically three-dimensional entities, without imposing any enforced factorization of the form $E = E_{2\text{D}}(x,y)E_{1\text{D}}(z)$. Moreover, strict TE-polarization of the fundamental A, B, C, and D modes is not assumed within the FEM framework, allowing for a considerable out-of-plane electric-field component $E_z(x,y,z)$ component.

Periodic boundary conditions are applied along the x - and y -axes, rendering the structure infinite in the lateral dimensions. The multilayer stack is terminated at the top and bottom by perfectly matched layers (PMLs). To minimize spurious mode overlap with the PMLs, a 200-nm air buffer layer is introduced above the ITO layer, whereas the lower PML

is placed directly beneath the n-type AlGaIn cladding layer, which has a thickness of 2000 nm.

D. Fourier modal method

The second rigorous method employed in this study is the FMM. In this approach, the square unit cell of the PhC and of the entire PCSEL structure is periodically extended along the x - and y -directions. The computational domain is terminated 200 nm above the ITO layer and 500 nm below the cladding-substrate interface, thereby ensuring sufficient optical isolation of vertically confined resonant guided modes. Optical excitation is implemented by means of an s- or p-polarized plane wave incident on the ITO layer. To excite the practically non-radiative quasi-BIC states of the single-lattice PhC, the plane-wave incidence angle is slightly tilted to $\theta = 0.01$. Although this condition does not correspond exactly to the second-order Γ point, it enables a fairly accurate estimation of the demanded eigenfrequencies. By contrast, in the Type II PCSEL all four modes are generally radiative; accordingly, excitation is performed using a normally incident plane wave ($\theta = 0$). Only for $ff_1 = 4\%$ and $\Delta = 0.5a$ was it necessary to introduce a small tilt angle ($\theta = 0.02$) to excite the high-Q mode pairs C, D, and A, B, respectively.

A parametric sweep of the excitation frequency yields reflection and transmission spectra of the structure, capturing both resonant dynamics associated with the embedded PhC grating and spectrally broader Fabry–Pérot-like longitudinal modes arising from multiple reflections at layer interfaces³². Once the fundamental quasi-TE modes A, B, C, and D are identified in the transmission (or equivalently, reflection) spectrum, their linewidths and associated quality factors are extracted via Lorentzian fitting. The corresponding radiation constants are then evaluated as $\alpha_i = \beta_0/Q_i$.

At large hole diameters in the Type I PCSEL, spectral overlap between the degenerate C and D modes and an unidentified resonance prevents a reliable extraction of the corresponding quality factors and, consequently, of the radiation constant $\alpha_{C,D}$. This issue is discussed in more detail in the following section.

III. RESULTS AND DISCUSSION

A. Single-lattice photonic crystal

In this section, we focus on the highly symmetric Type I pattern, for which 3D-CWT^{11,12} predicts non-radiative A and B modes ($\alpha_{A,B} = 0$) and degenerate C and D modes ($\bar{\nu}_C = \bar{\nu}_D$, $\alpha_C = \alpha_D$). Figures 2(a) and 3(a) show that, by construction of 3D-CWT, the photonic-crystal confinement factor Γ_{PhC} is identical for all four modes, whereas the other methods resolve mode-dependent electric-field profiles and, consequently, mode-dependent values of Γ_{PhC} . As evident from the plots, 3D-CWT systematically underestimates Γ_{PhC} when compared with the mode-specific confinement factors $\Gamma_{\text{PhC},A}$ and $\Gamma_{\text{PhC},B}$ obtained from the other methods. We preliminarily

attribute this discrepancy to the substantially smaller confinement factors of the more weakly confined C and D modes, which effectively contribute to the joint value of Γ_{PhC} within the 3D-CWT description. I-EIM agrees well with FEM in predicting Γ_{PhC} for mode A, but shows significant deviations for mode B, as evidenced in the corresponding plots.

Next, we observe a good agreement between FEM and FMM with regard to the modal effective indices n_{eff} , as shown in Figs. 2(b) and 3(b). 3D-CWT exhibits good agreement with FEM and FMM in predicting $n_{\text{eff},B}$, but shows reduced agreement for $n_{\text{eff},A}$. By contrast, I-EIM yields close agreement with the rigorous methods for the effective index of mode A, but shows noticeable deviations for mode B. The consistent agreement between FMM and FEM suggests an overall higher accuracy of these approximation-free methods.

Figures 4(a,b) show the modal radiation constants α_i as functions of the hole filling factor ff and the PhC thickness t_{PhC} . While $\alpha_{A,B}$ remain negligible for $ff < 14\%$, the radiation constants $\alpha_{C,D}$ attain significant values. As noted earlier, the accuracy of FMM deteriorates once the degenerate C and D modes spectrally overlap with an additional unidentified resonance for $ff \gtrsim 8\%$ at fixed t_{PhC} . This overlap leads to an artificial increase of $\alpha_{C,D}$, as observed in Fig. 4(a). Otherwise, the FMM-derived $\alpha_{C,D}$ closely follow their FEM-based counterpart. Note that all methods indicate convergence of $\alpha_{C,D}$ to zero as either ff or t_{PhC} approaches zero.

Furthermore, a primary breakdown of the symmetry protection of the quasi-BIC mode B manifests itself as a rapid increase in α_B at large hole diameters. Specifically, Fig. 4(a) shows that FMM predicts an abrupt rise of α_B at $ff > 16\%$, whereas FEM exhibits a more gradual exponential increase, that becomes visible around $ff \approx 12\%$, but is in fact starting at much smaller filling factors as illustrated in 5 with black curves on a logarithmic scale. An exponential increase of FEM-based α_A is also visible, but at a much slower pace.

To gain deeper insight into this behavior, we introduce the following absolute error function, which quantifies the discrepancy between a rigorous method and the CWT framework:

$$\delta = \sqrt{\frac{|\alpha_A - \alpha_{A,\text{rec}}|^2 + |\alpha_B - \alpha_{B,\text{rec}}|^2}{2}}, \quad (8)$$

where values $\alpha_{A,B;\text{rec}}$ denote best-fit parameters, reconstructed from the CWT framework using either FEM or FMM data as input. In the following, we focus on FEM-based values, which exhibit smoother behavior, and plot δ along with $\alpha_{A,B}$ and their CWT-compliant counterparts $\alpha_{A,B;\text{rec}}$ in Fig. 5. The logarithmic scale enhances visibility over a wide dynamic range. The results clearly show that both the error metric δ and the CWT-compliant radiation constants undergo an exponential increase starting at $ff \approx 14\%$. Overall, while the idealized 3D-CWT predicts perfect symmetry protection ($\alpha_{A,B} = 0$) and rigorous methods reveal exponentially growing radiation constants accompanied by an increasing asymmetry $\alpha_B - \alpha_A$, the hybridized CWT framework preserves symmetry protection only below $ff \approx 14\%$. For larger hole diameters, it instead predicts exponentially increasing radiative rates with nearly balanced levels ($\alpha_{A,\text{rec}} \approx \alpha_{B,\text{rec}}$).

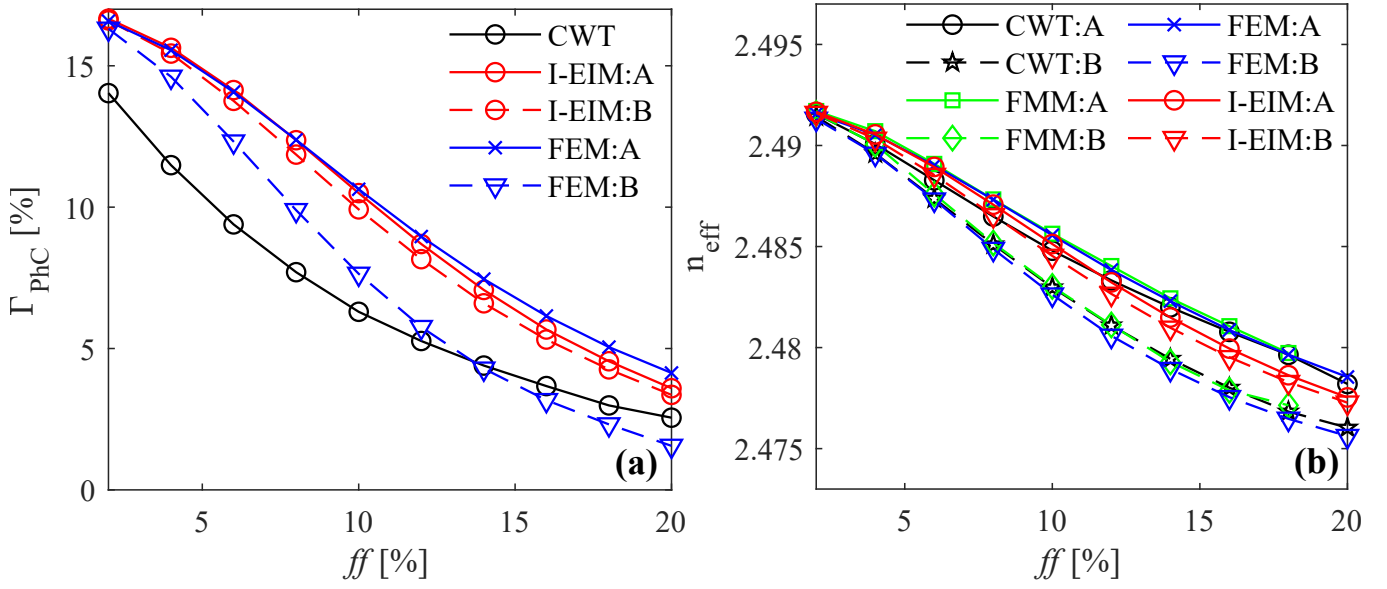


FIG. 2. (a) PhC confinement factors based on three methods as functions of the hole filling factor in the Type I PCSEL. 3D-CWT, unlike other methods, assumes a common vertical electric-field profile for all four modes, and thus Γ_{PhC} . t_{PhC} is fixed to 100 nm. (b) Effective indices as functions of ff , obtained as $\lambda_{A,B}/a$ for each corresponding method. The photonic-crystal thickness t_{PhC} is fixed at 100 nm.

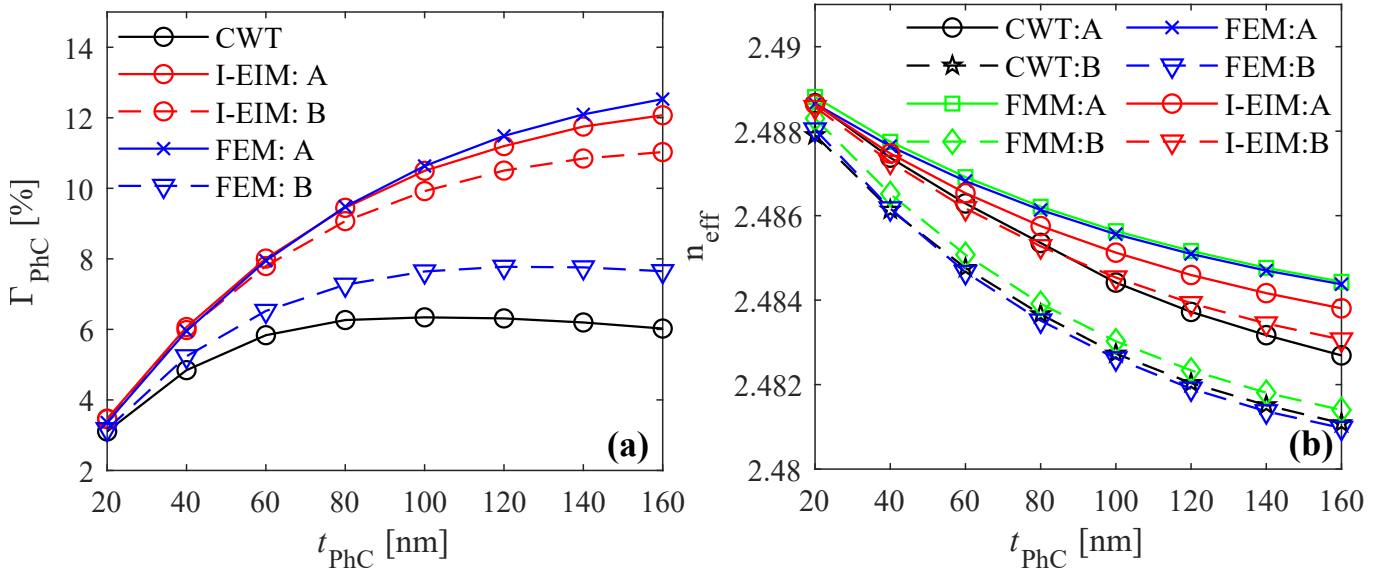


FIG. 3. (a) PhC confinement factors as functions of the PhC thickness, obtained by 3D-CWT, FEM, and I-EIM. ff is fixed to 10 %. (b) Effective indices as functions of t_{PhC} , obtained as $\lambda_{A,B}/a$ for each corresponding method. ff is fixed to 10 %.

It can be inferred that the CWT framework represents a compromise between the idealized 3D-CWT and fully rigorous approaches, which is manifested in a qualitative phase transition around $ff \approx 14\%$. The error metric δ provides a convenient indicator of this transition. Notably, even at large hole diameters, the CWT framework maintains an approximate balance between the radiation constants of modes A and B, suggesting that a weakened form of symmetry protection remains implicitly enforced.

In the following step, we evaluate coupling coefficients as described previously by feeding $\alpha_{C,D}$ and $\bar{v}_{A,B,C,D}$ into

Eqs. (1,2) and fitting the $\alpha_{A,B}$ and coupling coefficients within the CWT framework. In Figs. 6 and 3 the parameter κ_{1D} of FEM and FMM almost perfectly coincide at least for $ff < 10\%$. The increasing discrepancy observed at larger hole diameters can be attributed to the previously discussed unintended resonance overlap, which predominantly affects the FMM-based extraction of $\alpha_{C,D}$.

Figure 6 further demonstrates a relatively good agreement between FEM and FMM for κ_{2D} up to $ff \approx 16\%$. Overall, 3D-CWT provides a more accurate and consistent match to FEM and FMM results for κ_{1D} , whereas the I-EIM ap-

proach performs better in predicting κ_{2D+} . Nevertheless, for $ff > 10\%$, a growing deviation between I-EIM and the rigorous methods in κ_{2D+} becomes apparent. This deviation at large hole diameters may result from the system's gradual approach toward the principal phase-transition point, previously identified by δ , where the contrast between the radiation constants of quasi-BIC states predicted by effective-index-based and rigorous methods becomes significant.

Finally, in 3D-CWT, we incorporate either simplified Green functions of the form $G(z, z') \sim e^{-i\beta_z|z-z'|}/(2\beta_z)$ or generalized Green functions²⁸, accounting for secondary wave reflections at multilayer interfaces. Figs. 7(a,b) reveals that the latter ansatz leads to a divergence of coupling coefficients $\kappa_{1D,2D}$ as t_{PhC} exceeds ~ 100 nm. This divergence is associated with a pole of the Green functions themselves, arising from a combination of interface reflections, constructive interference between forward- and backward-propagating waves, and the absence of material absorption or alternative loss channels that would otherwise regularize that divergence. Such behavior is absent when using the simplified Green functions, which neglect secondary reflections at multiple interfaces. Importantly, both Green-function formulations yield comparable results as long as t_{PhC} does not exceed ~ 100 nm. However, it is also evident that κ_{2D} , computed using the generalized Green functions, begins to diverge near 80 nm, which corresponds approximately to the first-order Fabry-Pérot resonance in the PhC slab.

B. Double-lattice photonic crystal

Here we consider the Type II PCSEL, wherein the double-lattice pattern lowers the C_4 symmetry of the square lattice, thus breaking the symmetry protection and forcing quasi-BIC modes A and B to irradiate at the Γ point. In addition, the degeneracy between modes C and D gets lifted according to the CWT framework (see Eqs. (1,2)). All these changes are reflected in complex-valued coefficients κ_{1D} and κ_{2D} , and breaking of the symmetry condition $\kappa_{2D-} = \kappa_{2D+}$. In our simulated Type II system, we fix the filling factor ff_2 of the second hole to 4%, while tuning only the filling factor ff_1 of the first hole and the lateral distance Δ between holes, illustrated in Fig. 1(b).

First, Figs. 8(b) and 9(b) reveal a great agreement in n_{eff} between FEM and FMM. I-EIM agrees well in Γ_{PhC} and n_{eff} with rigorous methods only for mode A, provided that Δ is not too small. Similarly to the case of Type I PCSEL, 3D-CWT tends to underestimate Γ_{PhC} values in comparison to other methods. In general, the resonance contrast $n_{\text{eff,A}} - n_{\text{eff,B}}$ predicted by FEM and FMM remains unmatched by both effective-index-based methods, while the large FEM-based contrast $\Gamma_{\text{PhC,A}} - \Gamma_{\text{PhC,B}}$ is not reproduced by I-EIM.

Next, in Figs. 10(a,b), we plot the radiation constants of the four modes. First of all, it is striking that $\alpha_{C,D}$ from the rigorous methods agree much better with their CWT-based counterparts than $\alpha_{A,B}$, which are significantly larger in the rigorous approaches. In general, we observe a good agreement between FEM and FMM concerning all four α 's, despite some-

what noisy FMM-based values of α_B . One principal difference distinguishing the CWT approach from rigorous methods is the relation $\alpha_B > \alpha_A$, which holds in the former case but switches to $\alpha_A > \alpha_B$ in FEM and FMM cases.

In analogy with Type I PCSEL, we plot δ from Eq. 8 as a function of ff_1 and Δ , as shown in Fig. 11. For comparison, FMM-based values of δ are also provided along the cross-sections $\Delta = 0.46a$ and $ff_1 = 10\%$ in Figs. 12(a) and (b), respectively. As seen, the FEM- and FMM-based values of δ are generally in good agreement. However, Fig. 12(a) also reveals an anomalous increase of the FEM-based δ for $ff_1 > 6\%$ at $\Delta = 0.44a$, which is not reproduced by the corresponding FMM results. We attribute this behavior to a numerical artifact specific to the FEM implementation. Additional localized anomalies of unclear origin are also visible as isolated dark points in the colormap plot of Fig. 11.

The colormap plot shows a gradual increase of error δ with ff_1 and its decrease with Δ . While in the Type I PCSEL, we observed a triggered at $ff \approx 14\%$ exponential increase of δ mainly due to growing $\Delta\alpha_A$, here instead a permanent near-linear increase takes place due to a balanced contribution of $\Delta\alpha_A$ and $\Delta\alpha_B$. Since the rotational C_4 symmetry of a square lattice is broken by the double-lattice pattern, the symmetry protection of the quasi-BIC modes gets lifted, as evidenced by significant values of $\alpha_{A,B}$ in all methods, except when Δ approaches $0.5a$. On the other hand, a crucial difference becomes evident between the asymmetry ($\alpha_B > \alpha_A$) predicted by 3D-CWT and the CWT framework (see Figs. 13(a,b) for the FEM-based fits) and the opposite condition ($\alpha_A > \alpha_B$) obtained from the rigorous methods. In that sense, the error δ measures the magnitude of that asymmetry between quasi-BIC modes as well as the discrepancy between a rigorous method and the CWT framework. At the same time, in the Type II PCSEL, the monotonically increasing δ does not indicate qualitative phase transitions within the parameter range of interest. Assuming that the sign of asymmetry revealed by the rigorous methods is physically valid, this points to a fundamental limitation of the CWT framework, for which no obvious remedy exists to the best of our knowledge.

Next, we analyze the function $\delta(ff_1, \Delta)$ in Fig.11(a) in more detail. Note that δ becomes relatively small when the lateral hole distance Δ is above $0.44a$, or the first hole filling factor becomes comparable to the second one $ff_1 \sim ff_2$. Otherwise, the two-dimensional parameter is gradually increasing along ff_1 and Δ . For example, δ is crossing 10 cm^{-1} value at $ff_1 = 6\%$ and $\Delta = 0.30a$, but for $\Delta = 0.36a$ that threshold shifts to $ff_1 = 10\%$. Between these two points, the total hole filling factor $ff_1 + ff_2$ spans the range of $10 - 14\%$. For comparison, in the Type I case, the 10 cm^{-1} level is crossed by δ at $ff \approx 20\%$. For $\Delta > 0.44a$, the value of δ remains below 5 cm^{-1} at least in our range of interest $ff_1 \leq 15\%$, thus indicating a relatively weak asymmetry between modes A and B. Air holes with $ff_1 = 15\%$ and $ff_2 = 4\%$ come into contact at $\Delta \approx 0.23a$, implying that an additional buffer of roughly the average hole diameter $(d_1 + d_2)/2$ is required to reach $\Delta \approx 0.46a$ and thus to keep δ small. If the hole diameters are comparable ($ff_1 \approx ff_2 = 4\%$), then the threshold of 5 cm^{-1} is respected only for $\Delta > 0.36a$. The holes of that

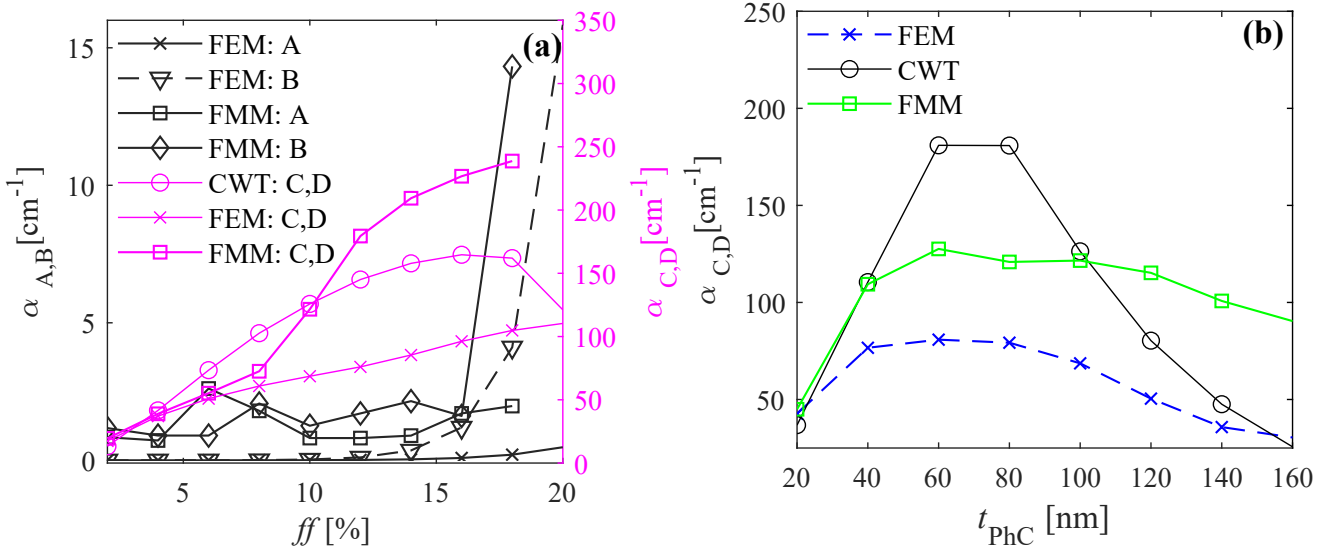


FIG. 4. (a) Radiation constants of the fundamental A,B,C and D modes, plotted in different scales (left and right y axes) as functions of the ff . $\alpha_{C,D}$ is not plotted at $ff = 20\%$ due to a strong spectral overlap of degenerate modes C, D with modes A and B. The PhC thickness is set to 100 nm. (b) Radiation constants of C and D modes, varying with PhC thickness. ff is fixed to 10%. Radiation constants of modes A and B are negligible and therefore omitted from the plot.

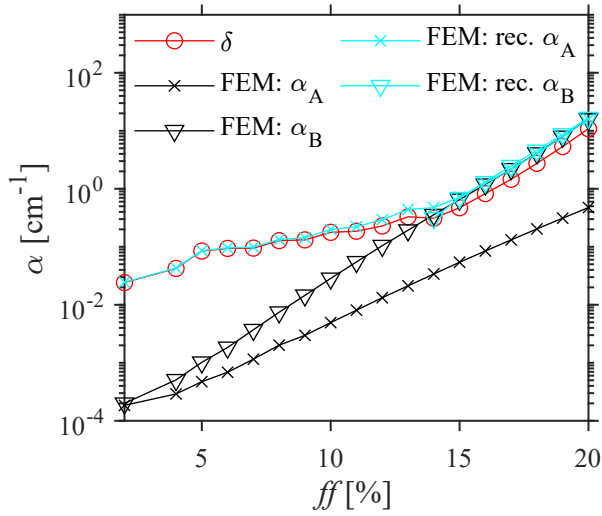


FIG. 5. Radiation constants $\alpha_{A,B}$ derived from FEM (black curves) and their CWT-compliant counterparts (cyan curves) as functions of ff . The error δ is shown in red.

small diameter would come into contact at $\Delta \approx 0.16a$, implying that an additional distance of $0.2a$, which is roughly equal to the hole diameter, is necessary to keep δ relatively small. In other words, as a qualitative rule, we propose that large hole diameters and bulk buffer gaps smaller than the average hole diameter lead to pronounced mode asymmetry and a substantial discrepancy between the rigorous methods and the CWT framework.

Next, Figs. 14(a,b) and 15(a,b) demonstrate 1D and 2D coupling coefficients plotted as functions of ff_1 and Δ , respectively. Again, we recognize a very good agreement in κ_{1D} be-

tween FEM and FMM, while 3D-CWT delivers a slightly elevated estimation. As already mentioned earlier, I-EIM does not allow us to extract complex-valued κ_{1D} and κ_{2D} . due to missing radiation constants. Concerning $\kappa_{2D\pm}$, the best match is observed, as before, between FEM and FMM. Here, an inaccuracy of 3D-CWT becomes more evident as it predicts significantly lower absolute values of $|\kappa_{2D\pm}|$. In contrast, I-EIM generates a more reliable estimation of κ_{2D+} , as it to some extent matches the rigorous methods. Specifically, I-EIM-based κ_{2D+} deviates from its counterparts obtained using rigorous methods when ff_1 exceeds $\sim 10\%$ at $\Delta = 0.46a$ (see Fig. 14(b)) or when Δ is reduced below $\sim 0.44a$ at $ff_1 = 10\%$ (Fig 15(b)). We assume that this disparity may reflect the gradual breakdown of the CWT framework, as discussed above. However, the exact relative position of I-EIM within the CWT framework cannot be fully assessed due to the absence of radiation constants and the associated complex-valued coupling coefficients for the Type II PCSEL.

Finally, the pronounced downward bending of FMM- and FEM-based curves $|\kappa_{2D\pm}|$ in Fig. 15(b), as Δ decreases from $0.5a$, is likely another indication of the growing disparity between predictions of the rigorous methods and the CWT framework. Note that coupling coefficients derived from the FEM and FMM eigenfrequency inputs are by definition CWT-compliant. Therefore, the asymmetry $|\kappa_{2D+}| > |\kappa_{2D-}|$ (in analogy with $\alpha_B > \alpha_A$) remains intact within both 3D-CWT and the hybridized CWT framework. Assuming that the asymmetry $\alpha_A > \alpha_B$ predicted by the rigorous methods is physically valid, we infer that a proper formulation of the CWT framework, if it exists, should reproduce this asymmetry in α and also enforce the swapped asymmetry $|\kappa_{2D-}| > |\kappa_{2D+}|$. In the current setting, however, we recognize that the asymmetry signs in $\alpha_{A,B}$ and $\kappa_{2D\pm}$ predicted by the hybridized CWT framework and 3D-CWT are likely physically

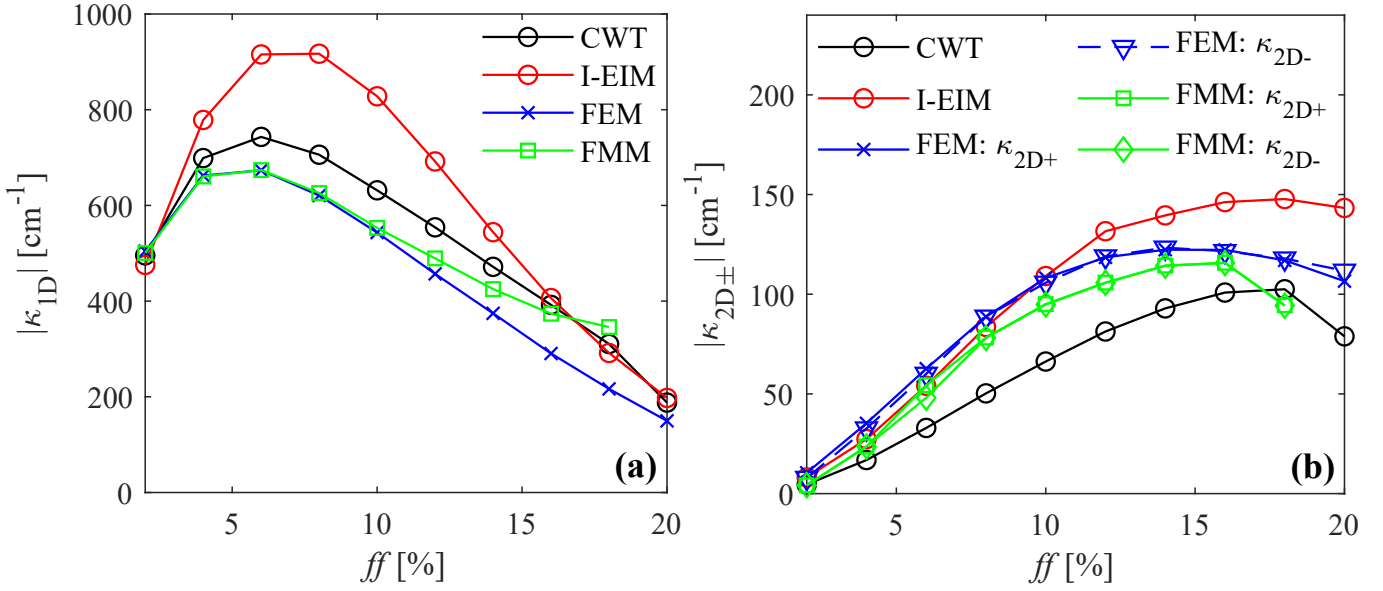


FIG. 6. (a) One-dimensional coupling coefficients as functions of ff , based on the corresponding four methods. PhC thickness is set to 100 nm. The data point of FMM is missing at $ff = 20\%$ due to a lack of $\alpha_{C,D}$ entering the chief Eqs.1. (b) Two-dimensional coupling coefficients as functions of ff , showing the expected equality $\kappa_{2D+} \approx \kappa_{2D-}$. The data point of FMM at $ff = 20\%$ is missing for the same reason as stated above. PhC thickness is fixed to 100 nm.

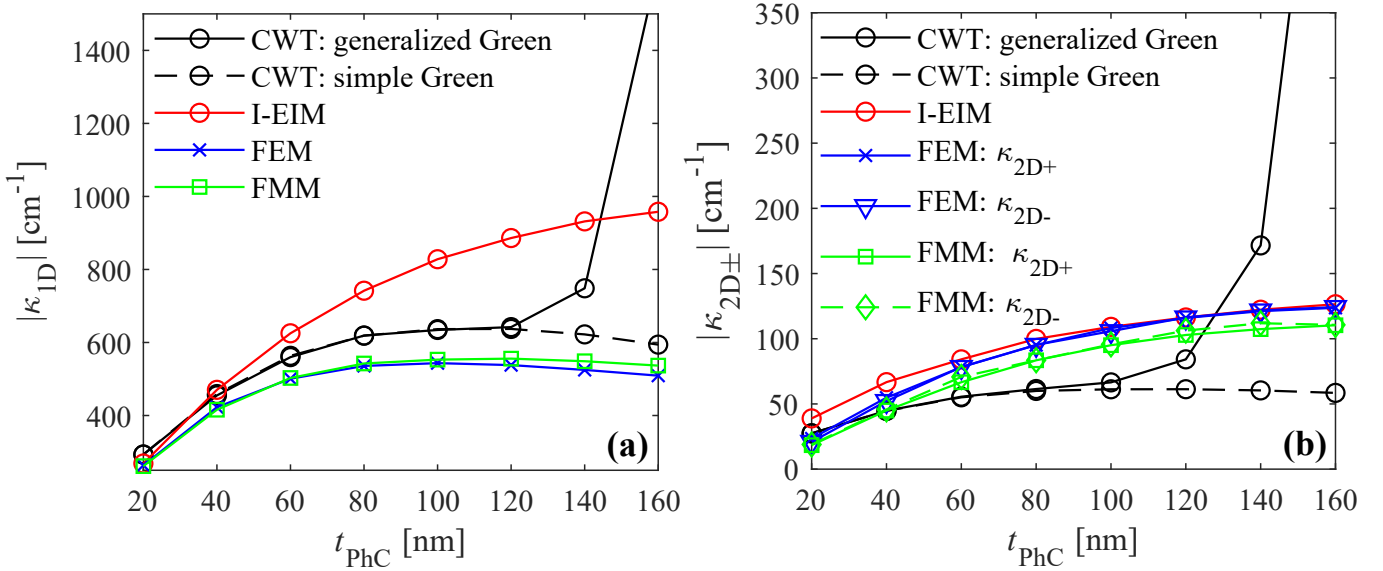


FIG. 7. (a) One- and (b) two-dimensional coupling coefficients, plotted as functions of PhC thickness at $ff = 10\%$. In 3D-CWT, a simplified exponential and, alternatively, a generalized Green function have been incorporated. The latter led to a clear divergence of both κ at $t_{\text{PhC}} \gtrsim 100$ nm.

invalid, as they contradict the mutually consistent results of the rigorous methods.

IV. CONCLUSION

In conclusion, we presented a comparative analysis of rigorous and effective index-based methods along with a hybridized CWT framework. We introduced a deviation metric

δ , which, in terms of band-edge quasi-BIC modes, quantifies the discrepancy between a rigorous method and the associated hybridized CWT theory framework.

For the single-lattice PCSEL, the hybridized CWT framework predicts a phase transition associated with the breakdown of symmetry protection of the quasi-BIC states at a hole filling factor of $ff \approx 14\%$, manifested by an exponential increase in δ . In contrast, neither the rigorous methods nor 3D-CWT alone reveal this transition, instead indicating a

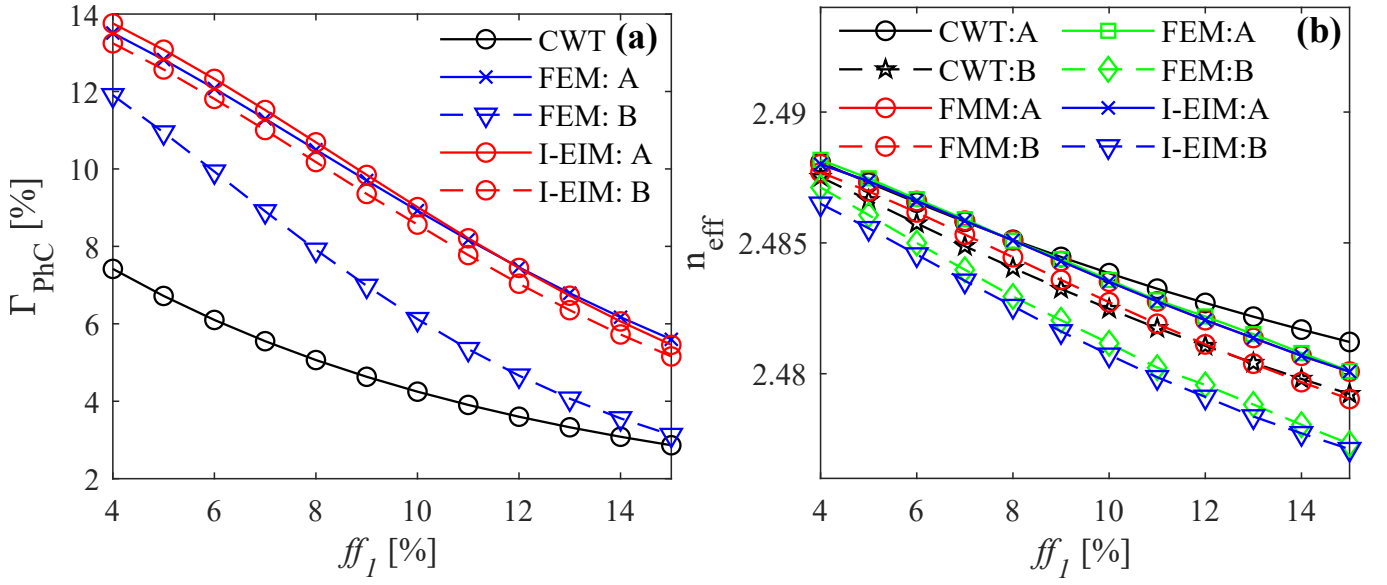


FIG. 8. (a) PhC confinement factors and (b) effective indices as functions of ff_1 of the first hole, derived from corresponding methods. ff_2 of the second hole is fixed to 4 %, while the lateral distance between holes is $\Delta = 0.46a$.

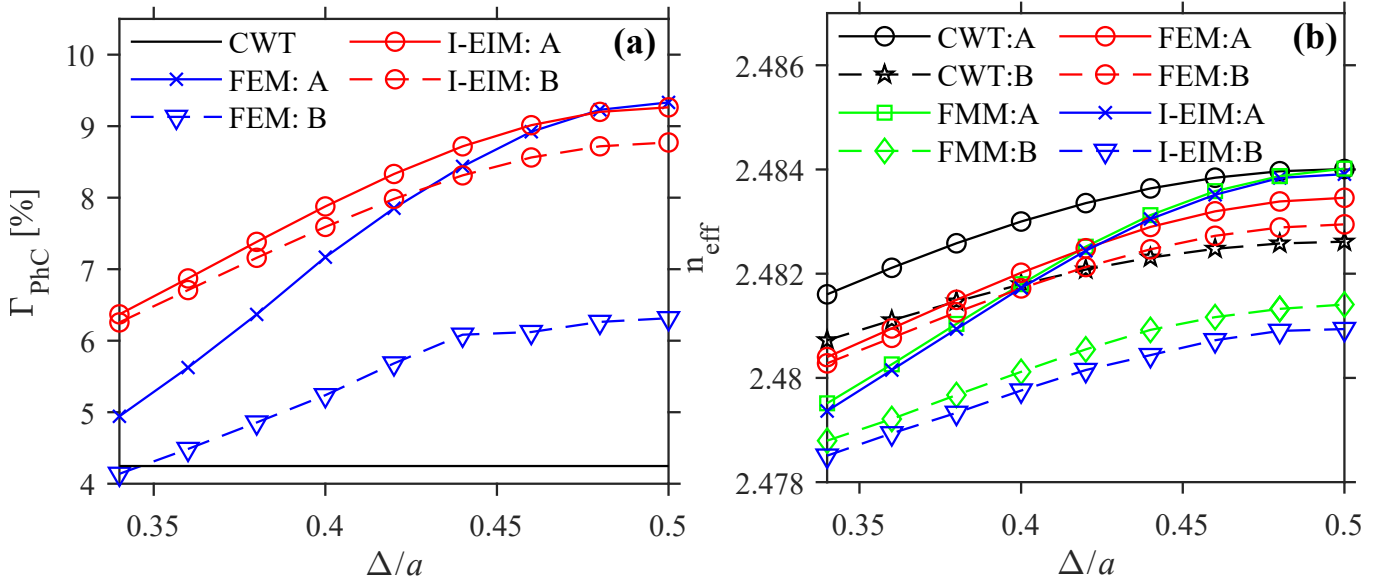


FIG. 9. (a) PhC confinement factors and (b) effective indices as functions of the lateral distance between air holes. ff_1 and ff_2 are set to 10 % and 4 %, respectively.

permanently symmetry-protected or symmetry-broken phase, respectively. Importantly, the hybridized CWT framework does not capture the growing asymmetry $\alpha_A - \alpha_B$ between the quasi-BIC states, as predicted by the rigorous methods, but it correctly identifies the qualitative change in their behavior at $ff \approx 14\%$.

In the double-lattice PCSEL, symmetry protection of the quasi-BIC modes is lifted as a result of symmetry breaking of the underlying square lattice. However, a non-zero deviation metric δ reveals that both the hybridized CWT framework and 3D-CWT predict the mode asymmetry $\alpha_B > \alpha_A$, which is opposite in sign to that obtained from rigorous methods. Accord-

ingly, the near-linear increase of δ as a function of ff_1 and Δ indicates a simultaneous increase in the asymmetry magnitude and in the discrepancy between the hybridized and rigorous approaches. Given the consistent agreement between FEM and FMM throughout this study, we conclude that the CWT-based prediction of a lossier mode B is likely misleading. Moreover, a proper formulation of the CWT framework, if achieved, is expected to yield the asymmetry $|\kappa_{2D-}| > |\kappa_{2D+}|$, which is opposite in sign to the condition currently enforced by the CWT framework.

Furthermore, as a qualitative rule, we found that δ becomes significant when either one of the hole diameters is sufficiently

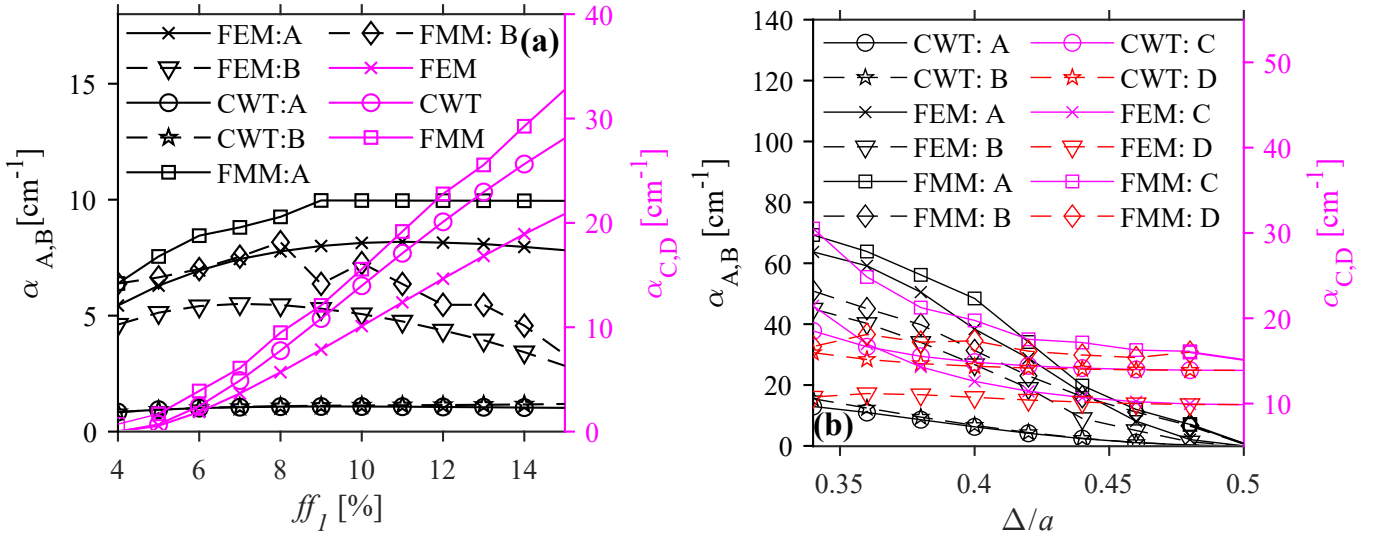


FIG. 10. Radiation constants of modes A, B (left y-axis) and C, D (right y-axis), plotted as functions of (a) ff_1 and (b) Δ based on four methods. $\Delta = 0.46a$ and $ff_1 = 10\%$ are fixed in plots (a) and (b), respectively.

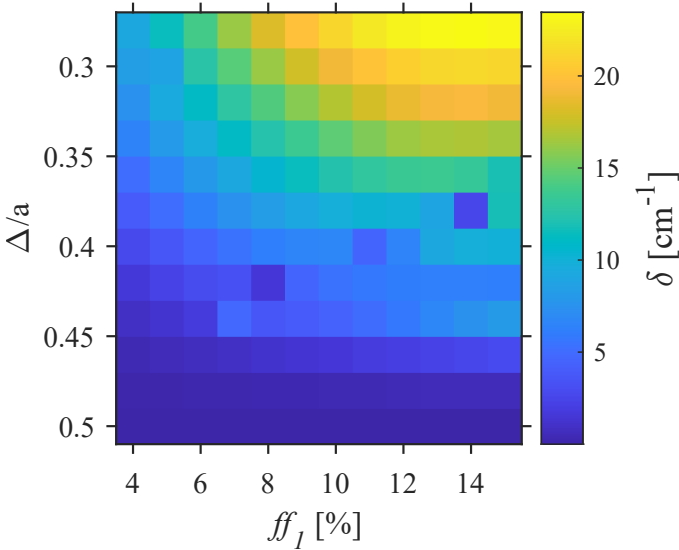


FIG. 11. The absolute deviation δ between FEM-based and CWT-compliant radiation constants of modes A and B, plotted as a colormap function of Δ and ff_1 .

large, or the bulk buffer gap between adjacent holes becomes comparable to the average hole diameter. Thus, the validity limits of the CWT framework for double-lattice PCSELs are qualitatively identified in terms of the largest hole diameters and the smallest bulk geometric features.

In addition, we included the iterated effective-index method in our analysis. Although its position relative to other methods cannot be fully assessed due to the absence of radiation constants in the modeled lossless system, we nevertheless observed a partial lopsided agreement with the FEM and FMM results. In particular, I-EIM provides overall more accurate

predictions of the real-valued $\kappa_{2D\pm}$, whereas 3D-CWT shows better agreement with rigorous methods for κ_{1D} . However, the relatively large contrast $\Gamma_{\text{PhC,A}} - \Gamma_{\text{PhC,B}}$ and the frequency splitting associated with $n_{\text{eff,A}} - n_{\text{eff,B}}$, as predicted by FEM and FMM, could not be consistently reproduced by either I-EIM or 3D-CWT.

Finally, the synergistic combination of the CWT framework with rigorous methods exposed the limits of validity of the coupled-wave theory, particularly in predicting the subtle behavior of quasi-BIC states. Nevertheless, the hybridized CWT framework correctly captured the qualitative phase transition and the symmetry-broken phase of quasi-BIC states in Type I and Type II PCSELs, respectively. In that sense, the mutually consistent rigorous methods, despite occasional numerical artefacts, provided a reliable benchmark for the CWT framework. The proposed comparative technique can be readily extended to a broader class of PCSEL architectures and photonic-crystal patterns, thereby enabling a deeper and more comprehensive understanding of these devices.

ACKNOWLEDGMENTS

The project was funded by the Deutsche Forschungsgemeinschaft (DFG, German Research Foundation) under Germany's Excellence Strategy – EXC-2123 QuantumFrontiers – 390837967. We acknowledge the financial support by the Volkswagen-Stiftung and the „Niedersächsisches Ministerium für Wissenschaft und Kultur“ within the Quantum Valley Lower Saxony Q1 project. Furthermore, the BMFTR funded project „QPIC“ within the Cluster4Future „QVLS iLabs“ supported this research. The authors thank Frederik Lüßmann, Daniel Stoll and Jana Hartmann for valuable support and discussions.

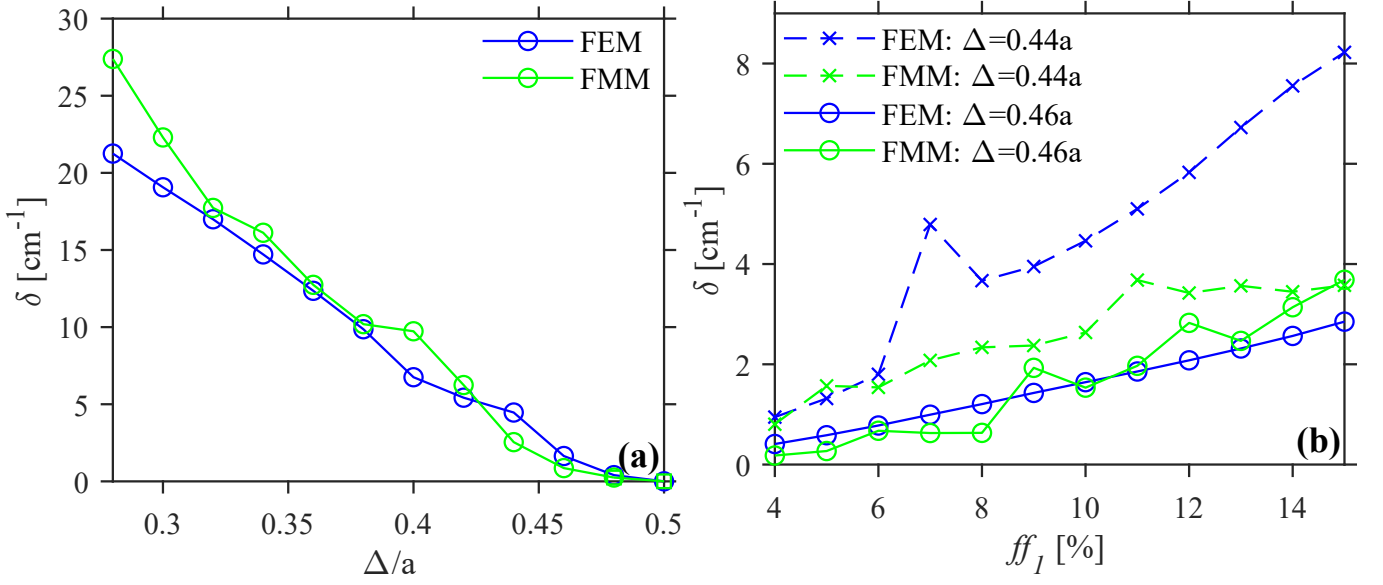


FIG. 12. The absolute deviation δ as a function of (a) Δ and (b) ff_1 , plotted for FEM- and FMM-based data.

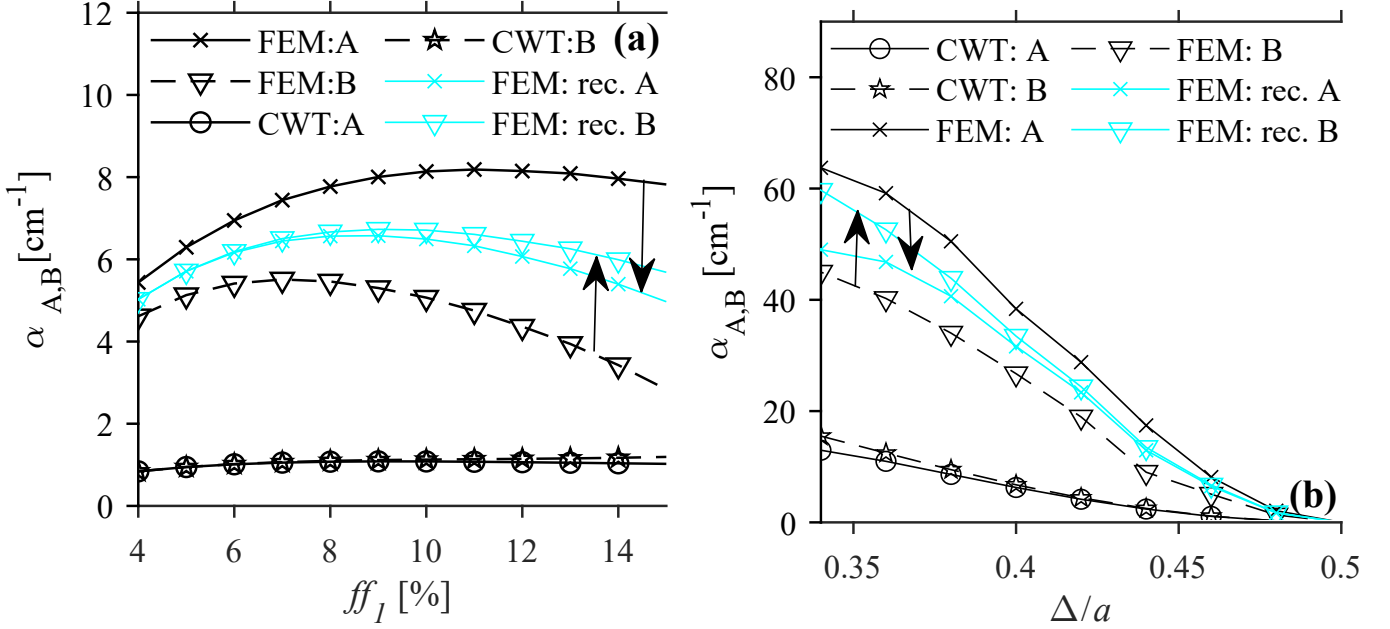


FIG. 13. Radiation constants of modes A and B as functions of (a) ff_1 and (b) Δ , derived from FEM and 3D-CWT as well as reconstructed from CWT framework combined with FEM-based data.

DATA AVAILABILITY STATEMENT

The data that support the findings of this study are available from the corresponding author upon reasonable request.

Appendix: Normalization of 2D coupling coefficients in I-EIM

Here we argue that once κ_{2D+} is derived from Eq. 7 or Eq. 3 using I-EIM-based eigenfrequencies, it must be normalized by the confinement factor Γ_{PhC} . To motivate this requirement,

we first consider the analytical CWT expression for κ_{2D+} (for details, see e.g.^{11,18}):

$$\kappa_{2D+} = \frac{k_0^2}{2\beta_0} \sum_{\sqrt{m^2+n^2}>1} \xi_{1-m,-n} \zeta_{y,m,n}^{(0,1)}, \quad (\text{A1})$$

where k_0 is the free-space wavenumber, $\beta_0 = 2\pi/a$, $\xi_{m,n}$ denote the spatial Fourier coefficients of the patterned PhC relative permittivity $\epsilon_{\text{PhC}}(x,y) = \epsilon_{\text{avg}} + \sum_{m,n \neq 0} \xi_{m,n} e^{-i\beta_0(mx+ny)}$ with ϵ_{avg} representing the spatially averaged permittivity of the PhC layer. According to¹¹, $\zeta_{y,m,n}^{(0,1)}$ takes the form:

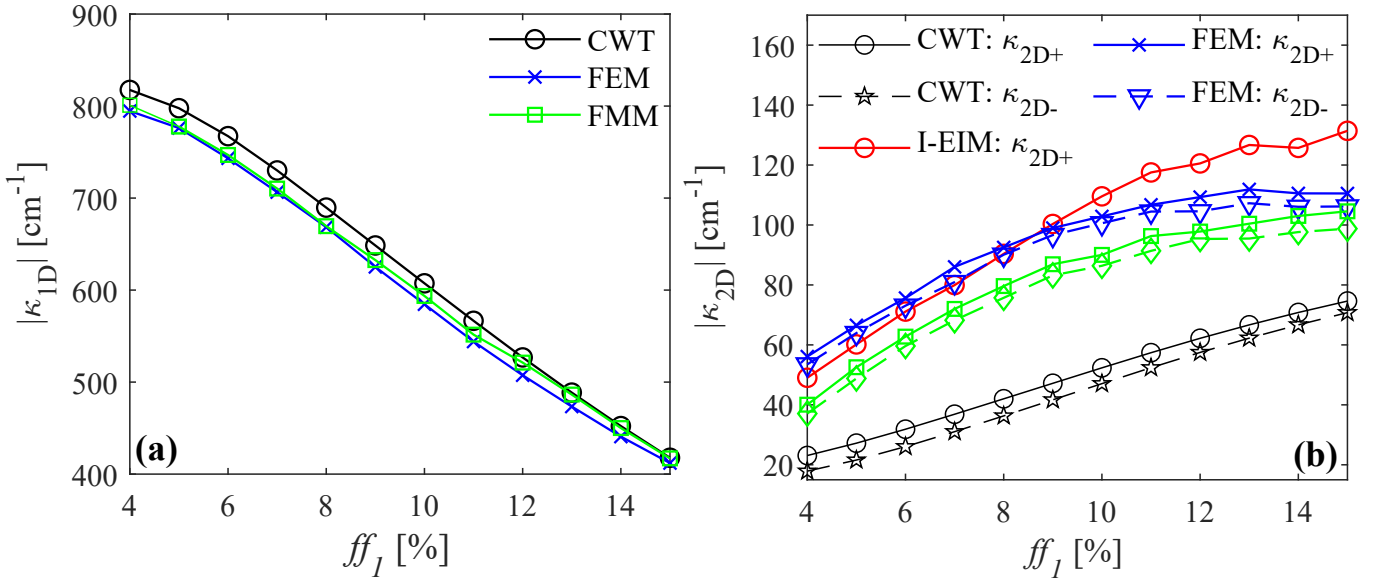


FIG. 14. (a) One- and (b) two-dimensional coupling coefficients, plotted as functions of ff_1 based on different methods. In plot (a), only 3D-CWT, FEM, and FMM are represented, while in plot (b), additionally, the I-EIM-based κ_{2D+} is plotted.

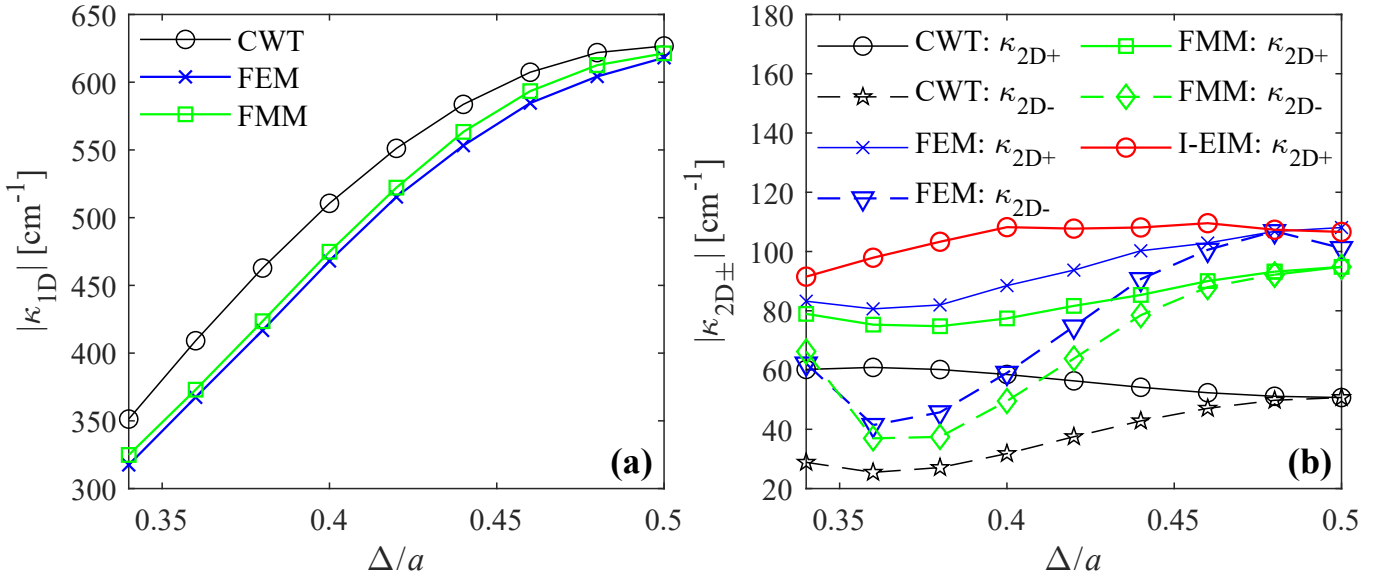


FIG. 15. (a) One- and (b) two-dimensional coupling coefficients, plotted as functions of Δ based on different methods. I-EIM lacking any data about radiation constants is eligible only for defining κ_{2D+} in plot (b).

$$\begin{aligned} \zeta_{y,m,n}^{(0,1)} \sim & -k_0 \iint \xi_{m,n-1}(z) G_{m,n}(z, z') E_{1D}(z) E_{1D}^*(z') dz' dz \\ & - \int \frac{\xi_{m,n-1}(z) |E_{1D}(z)|^2}{\epsilon_{\text{avg}}(z)} dz \end{aligned} \quad (\text{A2})$$

where the integrals are evaluated over the entire multi-layer structure, $E_{1D}(z)$ denotes the effective one-dimensional electric-field profile, and $G_{m,n}(z, z')$ are the Green's functions defined in¹¹.

Within the 3D-CWT method, the terms $\xi_{m,n}(z)$ are proportional to the material contrast $\Delta\epsilon(z)$, and are therefore nonzero only inside the PhC region. Consequently, the integrals in the above expression receive contributions exclusively from the PhC layer and vanish outside it. The field amplitude $|E_{1D}(z)|$ within the PhC layer can be approximated as $\sqrt{\Gamma_{\text{PhC}}}$, so that both integrals in Eq. A1 scale proportionally to $\Delta\epsilon_{\text{PhC}}\Gamma_{\text{PhC}}$. As a result, the 2D coupling coefficient consists of summation terms sharing the common factor $\Delta\epsilon_{\text{PhC}}^2\Gamma_{\text{PhC}}$.

In the I-EIM method, the situation is different. There, the coefficients $\xi_{m,n}$ are independent of z , and the material contrast is effectively averaged over the entire multi-

layer stack. As a result, instead of the localized dependence $\xi_{m,n}(z \in \text{PhC}) \sim \Delta\epsilon_{\text{PhC}}$, one obtains a uniform coefficient $\xi_{m,n} \sim \Gamma_{\text{PhC}}\Delta\epsilon_{\text{PhC}}$, since the PhC layer contributes only a fraction Γ_{PhC} to the averaged permittivity contrast. Consequently, the integrals in Eq. A1 extend over the entire PCSEL structure, yielding $\zeta_{y,m,n}^{(0,1)} \sim \Delta\epsilon_{\text{PhC}}\Gamma_{\text{PhC}}$, as in the 3D-CWT case.

However, κ_{2D+} contains additional prefactors $\xi_{1-m,-n} \sim \Gamma_{\text{PhC}}\Delta\epsilon_{\text{PhC}}$, so that each term in the summation for the 2D coupling coefficient scales as $\sim \Gamma_{\text{PhC}}^2\Delta\epsilon_{\text{PhC}}^2$. Thus, in contrast to 3D-CWT, an extra factor of Γ_{PhC} appears, which must be removed by an appropriate renormalization. The same reasoning applies to κ_{2D-} , but not to κ_{1D} , whose structure is analogous to $\zeta_{y,m,n}^{(0,1)}$, but lacks an additional prefactor of the form $\xi_{m,n}$. Therefore, the issue of the redundant Γ_{PhC} factor does not arise for the one-dimensional coupling coefficient.

- ¹M. Imada, S. Noda, A. Chutinan, T. Tokuda, M. Murata, and G. Sasaki, "Coherent two-dimensional lasing action in surface-emitting laser with triangular-lattice photonic crystal structure," *Applied physics letters* **75**, 316–318 (1999).
- ²M. Meier, A. Mekis, A. Dodabalapur, A. Timko, R. Slusher, J. Joannopoulos, and O. Nalamasu, "Laser action from two-dimensional distributed feedback in photonic crystals," *Applied Physics Letters* **74**, 7–9 (1999).
- ³S. Noda, T. Inoue, M. Yoshida, J. Gellela, M. D. Zoysa, and K. Ishizaki, "High-power and high-beam-quality photonic-crystal surface-emitting lasers: a tutorial," *Advances in Optics and Photonics* **15**, 977–1032 (2023).
- ⁴K. Ishizaki, M. De Zoysa, and S. Noda, "Progress in photonic-crystal surface-emitting lasers," in *Photonics*, Vol. 6 (MDPI, 2019) p. 96.
- ⁵M. Pan, C. Gautam, Y. Chen, T. Rotter, G. Balakrishnan, and W. Zhou, "Recent advances in photonic crystal surface emitting lasers," *IEEE Journal of Selected Topics in Quantum Electronics* **31**, 1–8 (2024).
- ⁶S. Noda, M. Yoshida, T. Inoue, M. De Zoysa, K. Ishizaki, and R. Sakata, "Photonic-crystal surface-emitting lasers," *Nature Reviews Electrical Engineering* **1**, 802–814 (2024).
- ⁷R. Sakata, K. Ishizaki, M. De Zoysa, K. Kitamura, T. Inoue, J. Gellela, and S. Noda, "Photonic-crystal surface-emitting lasers with modulated photonic crystals enabling 2d beam scanning and various beam pattern emission," *Applied Physics Letters* **122** (2023).
- ⁸S. Katsuno, M. Yoshida, T. Inoue, M. De Zoysa, R. Hatsuda, K. Ishizaki, and S. Noda, "Design and experimental demonstration of photonic-crystal lasers with multijunction active layers," *Applied Physics Express* **17**, 122004 (2024).
- ⁹S. Ishimura, R. Morita, T. Inoue, K. Nishimura, H. Takahashi, T. Tsuritani, M. De Zoysa, K. Ishizaki, M. Suzuki, and S. Noda, "Proposal and demonstration of free-space optical communication using photonic crystal surface-emitting lasers," *Journal of Lightwave Technology* **41**, 3688–3694 (2023).
- ¹⁰H. Huang, C. Yang, H. Li, and Z. Zhang, "Unveiling the potential of photonic crystal surface emitting lasers: a concise review," *Semiconductor Science and Technology* (2025).
- ¹¹Y. Liang, C. Peng, K. Sakai, S. Iwahashi, and S. Noda, "Three-dimensional coupled-wave model for square-lattice photonic crystal lasers with transverse electric polarization: A general approach," *Physical Review B—Condensed Matter and Materials Physics* **84**, 195119 (2011).
- ¹²Y. Liang, C. Peng, K. Sakai, S. Iwahashi, and S. Noda, "Three-dimensional coupled-wave analysis for square-lattice photonic crystal surface emitting lasers with transverse-electric polarization: finite-size effects," *Optics express* **20**, 15945–15961 (2012).
- ¹³Y. Liang, C. Peng, K. Ishizaki, S. Iwahashi, K. Sakai, Y. Tanaka, K. Kitamura, and S. Noda, "Three-dimensional coupled-wave analysis for triangular-lattice photonic-crystal surface-emitting lasers with transverse-electric polarization," *Optics express* **21**, 565–580 (2013).
- ¹⁴C. Peng, Y. Liang, K. Sakai, S. Iwahashi, and S. Noda, "Three-dimensional coupled-wave theory analysis of a centered-rectangular lattice photonic crystal laser with a transverse-electric-like mode," *Physical Review B—Condensed Matter and Materials Physics* **86**, 035108 (2012).
- ¹⁵M. Yoshida, M. De Zoysa, K. Ishizaki, Y. Tanaka, M. Kawasaki, R. Hatsuda, B. Song, J. Gellela, and S. Noda, "Double-lattice photonic-crystal resonators enabling high-brightness semiconductor lasers with symmetric narrow-divergence beams," *Nature materials* **18**, 121–128 (2019).
- ¹⁶M. Yoshida, S. Katsuno, T. Inoue, J. Gellela, K. Izumi, M. De Zoysa, K. Ishizaki, and S. Noda, "High-brightness scalable continuous-wave single-mode photonic-crystal laser," *Nature* **618**, 727–732 (2023).
- ¹⁷K. Emoto, T. Koizumi, M. Hirose, M. Jutori, T. Inoue, K. Ishizaki, M. De Zoysa, H. Togawa, and S. Noda, "Wide-bandgap gan-based watt-class photonic-crystal lasers," *Communications Materials* **3**, 72 (2022).
- ¹⁸T. Inoue, M. Yoshida, J. Gellela, K. Izumi, K. Yoshida, K. Ishizaki, M. De Zoysa, and S. Noda, "General recipe to realize photonic-crystal surface-emitting lasers with 100-w-to-1-kw single-mode operation," *Nature Communications* **13**, 3262 (2022).
- ¹⁹M. De Zoysa, M. Yoshida, B. Song, K. Ishizaki, T. Inoue, S. Katsuno, K. Izumi, Y. Tanaka, R. Hatsuda, J. Gellela, *et al.*, "Thermal management for cw operation of large-area double-lattice photonic-crystal lasers," *Journal of the Optical Society of America B* **37**, 3882–3887 (2020).
- ²⁰T. Inoue, R. Morita, M. Yoshida, M. De Zoysa, Y. Tanaka, and S. Noda, "Comprehensive analysis of photonic-crystal surface-emitting lasers via time-dependent three-dimensional coupled-wave theory," *Physical Review B* **99**, 035308 (2019).
- ²¹S. Katsuno, T. Inoue, M. Yoshida, M. D. Zoysa, K. Ishizaki, and S. Noda, "Self-consistent analysis of photonic-crystal surface-emitting lasers under continuous-wave operation," *Optics Express* **29**, 25118–25132 (2021).
- ²²R. Morita, T. Inoue, M. Yoshida, K. Enoki, M. De Zoysa, K. Ishizaki, and S. Noda, "Demonstration of high-power photonic-crystal surface-emitting lasers with 1-khz-class intrinsic linewidths," *Optica* **11**, 333–339 (2024).
- ²³R. Morita, S. Ishimura, T. Inoue, K. Nishimura, H. Takahashi, T. Tsuritani, M. De Zoysa, K. Ishizaki, M. Suzuki, and S. Noda, "High-speed high-power free-space optical communication via directly modulated watt-class photonic-crystal surface-emitting lasers," *Optica* **11**, 971–979 (2024).
- ²⁴K. Hirose, Y. Liang, Y. Kurosaka, A. Watanabe, T. Sugiyama, and S. Noda, "Watt-class high-power, high-beam-quality photonic-crystal lasers," *Nature photonics* **8**, 406–411 (2014).
- ²⁵B. King, H. Wenzel, E. Kuhn, M. Radziunas, and P. Crump, "Design of very-large area photonic crystal surface emitting lasers with an all-semiconductor photonic crystal," *Optics Express* **32**, 44945–44957 (2024).
- ²⁶M. Radziunas, E. Kuhn, H. Wenzel, B. King, and P. Crump, "Optical mode calculation in large-area photonic crystal surface-emitting lasers," *IEEE Photonics Journal* **16**, 1–9 (2024).
- ²⁷W. Ke, T. Li, Y. He, H. Chen, Z. Jiang, X. Lu, H.-L. Cai, Q. Qin, and X. Wu, "Design of red pcseles with rotatable double-ellipse for single-mode and high-power operation," Available at SSRN 5400511.
- ²⁸C. Peng, Y. Liang, K. Sakai, S. Iwahashi, and S. Noda, "Coupled-wave analysis for photonic-crystal surface-emitting lasers on air holes with arbitrary sidewalls," *Optics Express* **19**, 24672–24686 (2011).
- ²⁹Y. Itoh, T. Aoki, K. Fujii, H. Yoshinaga, N. Fujiwara, K. Takada, M. Ogasawara, Y. Sawada, H. Yagi, M. Yanagisawa, *et al.*, "High-power and high-efficiency operation of 1.3 μm -wavelength inp-based photonic-crystal surface-emitting lasers with metal reflector," *Optics Express* **32**, 12520–12527 (2024).
- ³⁰B. Lang, P. D. Sewell, A. Vukovic, K. Boylan, S. Rihani, D. Moodie, R. Spalding, N. Hattasan, and G. Berry, "Mode switching in photonic crystal surface emitting lasers with back reflectors and holes of varying depths," *Optics Express* **33**, 35257–35269 (2025).
- ³¹J. Xu, D. McCulloch, and M. D. Charlton, "Modeling full pcseles and vcseles using modified rigorous coupled-wave analysis," *Optics Express* **32**, 22169–22180 (2024).
- ³²A. Y. Song, A. R. K. Kalapala, W. Zhou, and S. Fan, "First-principles simulation of photonic crystal surface-emitting lasers using rigorous coupled wave analysis," *Applied Physics Letters* **113** (2018).
- ³³Q. Liu, M. Meng, S. Ma, and M. Feng, "Design of double-lattice gan-pcsele based on triangular and circular holes," *Optics Express* **31**, 43615–43629 (2023).
- ³⁴L. Persson, M. Riedel, Å. Haglund, and U. T. Schwarz, "Finite-size effects in photonic-crystal surface-emitting lasers: critical discussion of different approximations," *Optics Express* **33**, 53098–53116 (2025).
- ³⁵J. Liu, Y. Gao, P. Ivanov, P. Harvey, and R. Hogg, "Probabilistic markov chain modeling of photonic crystal surface emitting lasers," *Ap-*

- plied Physics Letters **123** (2023).
- ³⁶J. Liu, X. Zhao, Z. Bian, P. Harvey, S. Watson, S. J. Sweeney, and R. Hogg, “Interdependence of parasitic losses in photonic crystal surface emitting lasers,” *AIP Advances* **15** (2025).
- ³⁷B. Lang, P. D. Sewell, A. Vukovic, K. Boylan, S. Rihani, D. Moodie, R. Spalding, N. Hattasan, and G. Berry, “Assessment and extension of rapid design tools for modeling photonic crystal surface-emitting lasers,” *Journal of the Optical Society of America B* **42**, 1123–1130 (2025).
- ³⁸W.-H. Hsieh, K.-B. Hong, C.-H. Lin, C.-Y. Yang, T.-C. Lu, and C.-Y. Huang, “Impact of air hole geometry on the performance of InGaN/GaN photonic crystal surface-emitting lasers,” *IEEE Journal of Selected Topics in Quantum Electronics* **32**, 1–6 (2025).
- ³⁹K. Ishizaki, R. Sakata, K. Iwata, T. Inoue, M. De Zoysa, A. Imamura, M. Yoshida, R. Hatsuda, J. Gellera, and S. Noda, “Enhancement of slope efficiency of a dually modulated photonic-crystal surface-emitting laser over a wide range of emission angles by introducing a backside reflector,” *Journal of the Optical Society of America B* **40**, 326–333 (2023).
- ⁴⁰C. W. Hsu, B. Zhen, A. D. Stone, J. D. Joannopoulos, and M. Soljačić, “Bound states in the continuum,” *Nature Reviews Materials* **1**, 16048 (2016).
- ⁴¹J. Lee, B. Zhen, S.-L. Chua, W. Qiu, J. D. Joannopoulos, M. Soljačić, and O. Shapira, “Observation and differentiation of unique high- q optical resonances near zero wave vector in macroscopic photonic crystal slabs,” *Physical Review Letters* **109**, 067401 (2012).
- ⁴²H. Zhao, X. Cao, Q. Dong, C. Song, L. Wang, and L. Gao, “Large-area silicon photonic crystal supporting bound states in the continuum and optical sensing formed by nanoimprint lithography,” *Nanoscale Advances* **5**, 1291–1298 (2023).
- ⁴³S. Li, L. Huang, H. Zhong, M. Ning, L.-E. Zhang, Y. Yin, Y. Cheng, and L. Li, “Observation of multiple quasi-bound states in the continuum by symmetry breaking in a photonic crystal slab,” *Photonics Research* **13**, 968–975 (2025).
- ⁴⁴S. G. Johnson and J. D. Joannopoulos, “Block-iterative frequency-domain methods for Maxwell’s equations in a planewave basis,” *Optics Express* **8**, 173–190 (2001).
- ⁴⁵M. N. Robinson, S. J. Sweeney, and R. A. Hogg, “Two-dimensional coupled wave theory for triangular lattice TM-polarised photonic crystal surface emitting lasers,” *IEEE Journal of Selected Topics in Quantum Electronics* **31**, 1–11 (2024).